HHS Public Access

Author manuscript

Curr Biol. Author manuscript; available in PMC 2023 January 24.

Published in final edited form as:

Curr Biol. 2022 January 24; 32(2): 315–328.e4. doi:10.1016/j.cub.2021.11.005.

Dendro-somatic synaptic inputs to ganglion cells contradict receptive field and connectivity conventions in the mammalian retina

William N. Grimes[1,†], **Miloslav Sedlacek**[1,†], **Morgan Musgrove**[1,2,3], **Amurta Nath**[1], **Hua Tian**[1], **Mrinalini Hoon**[4], **Fred Rieke**[5], **Joshua H. Singer**[2], **Jeffrey S. Diamond**[1,*]

[1]Synaptic Physiology Section, National Institute of Neurological Disorders and Stroke, National Institutes of Health, Bethesda, MD 20892

[2]Department of Biology, University of Maryland, College Park, MD 20742

[3]Program in Neuroscience and Cognitive Science, University of Maryland, College Park, MD 20742

[4]Department of Ophthalmology and Visual Sciences, University of Wisconsin School of Medicine and Public Health, Madison, WI 53706

[5]Department of Physiology and Biophysics, University of Washington, Seattle, WA 98195

Summary

The morphology of retinal neurons strongly influences their physiological function. Ganglion cell (GC) dendrites ramify in distinct strata of the inner plexiform layer (IPL) so that GCs responding to light increments (ON) or decrements (OFF) receive appropriate excitatory inputs. This vertical stratification prescribes response polarity and ensures consistent connectivity between cell types, whereas the lateral extent of GC dendritic arbors typically dictates receptive field (RF) size. Here, we identify circuitry in mouse retina that contradicts these conventions. AII amacrine cells are interneurons understood to mediate “cross-over” inhibition by relaying excitatory input from the ON layer to inhibitory outputs in the OFF layer. Ultrastructural and physiological analyses show, however, that some AIIs deliver powerful inhibition to OFF GC somas and proximal dendrites in the ON layer, rendering the inhibitory RFs of these GCs smaller than their dendritic arbors. This OFF pathway, avoiding entirely the OFF region of the IPL, challenges several tenets of retinal circuitry. These results also indicate that subcellular synaptic organization can vary within a single population of neurons according to their proximity to potential postsynaptic targets.

*Lead contact: diamondj@ninds.nih.gov.

†These authors contributed equally.

Author Contributions

Conceptualization, WNG, MH, FR, JHS and JSD; Methodology, WNG, JHS, JSD; Investigation, MS, WNG, MH, AN, HT, MH, JHS; Writing – Original Draft, JSD; Writing – Review & Editing, MS, WNG, MH, JHS, JSD; Visualization – WNG, MH, MM, JHS, JSD; Supervision – WNG, JHS, JSD; Funding acquisition, MH, FR, JHS, JSD.

Declaration of Interests

The authors declare no competing interests.

eTOC blurb

AII amacrine cells provide crossover inhibition to OFF-responding retinal circuits. Here, Grimes, et al. show that the synaptic organization of AIIs is altered when the cells overlap in space with OFFα ganglion cell somas. AII synaptic organization is, therefore, heterogeneous and depends on proximity to specific postsynaptic partners.

Introduction

AII ("A-two") amacrine cells (ACs) play diverse signaling roles in the mammalian retina[1,2]. During night (scotopic) vision, AIIs relay input from rod bipolar cells (RBs) to ON and OFF cone bipolar cell (CB) axon terminals that contact GCs (Figure 1A). ON signals from RBs are preserved via electrical synapses to ON CBs and inverted via glycinergic inhibitory synapses to OFF CBs[3-6]. This circuitry reliably transmits scotopic signals to ON GCs[7], but AII inhibition of OFF CBs exerts little influence on OFF GC signaling near visual threshold[8]. AIIs also contact OFF GCs directly[9-13], but synaptic connections between individual AII-GC pairs in the OFF layer of the IPL are weak[13,14]. It therefore remains unclear how scotopic visual signals are transmitted most reliably to OFF GCs.

Here, ultrastructural analysis of mouse retina indicates that AIIs make chemical synapses deep in the IPL and ganglion cell layer (GCL) onto the proximal dendrites, somas, and axons of GCs. We find that these AII outputs selectively target sustained and transient OFFα (s-OFFα and t-OFFα) GCs, subtypes that convey temporally precise visual signals to the superior colliculus and visual thalamus in mammals[15-19]. These synapses are made by a small subset of AIIs whose arboreal dendrites encounter OFFα somas, and they are made selectively onto OFFαs. These AII outputs arise from distal dendrites, close to where AIIs receive excitatory inputs from RBs, promoting efficient signal transfer. Fluorescence imaging and electrophysiology experiments indicate that depolarizing stimuli elevate [Ca^{2+}] in AII arboreal dendritic compartments and elicit inhibitory postsynaptic currents (IPSCs) in OFFα GCs. Scotopic light-evoked IPSCs in s-OFFα GCs exhibit narrow RFs that do not correlate with dendritic arbor dimensions. Together, these results show that OFFα GCs receive powerful somatic inhibition that influences RF properties and that AII synaptic organization is heterogeneous.

Results

In the canonical view of mammalian retinal circuitry[1], AIIs make all their glycinergic outputs onto CB axon terminals and GC dendrites from their lobular dendrites in sublamina a (the "OFF layer") of the IPL[3,9-13]; Figure 1A). AIIs also extend arboreal dendrites deep into sublamina b (the "ON layer"), where they receive excitatory inputs from RBs and make electrical synapses onto ON CB terminals[3,5,6,20,21] but express chemical synapses only rarely[22]. AII arboreal dendrites occasionally extend into the ganglion cell layer (GCL[23]), where their function is unknown.

AIIs selectively contact OFFαs in the ON layer

In a conventionally stained serial block-face scanning electron microscopy (SBFSEM) volume from mouse retina[24], some AIIs contained active zones within their arboreal dendrites that were presynaptic to GC dendrites and somas (e.g., Figure 1B,C; Figure S1). We followed postsynaptic GC processes and completely traced two GCs that appeared, based on dendritic stratification and soma size, to be s-OFFα and t-OFFα GCs (Figure 1E,K,L; Table S1). One of each OFFα GC was identified within the dataset, consistent with s-OFFα and t-OFFα density in rat retina[25]. Notably, no other GCs were found to be postsynaptic to ON/GCL synapses from AIIs.

We annotated all synaptic inputs onto the s-OFFα and t-OFFα (Figure 1D,H, S2; Table S1), then traced the presynaptic process at each inhibitory input to determine whether it arose from an AII (see STAR Methods). Each presynaptic AII was traced sufficiently to identify all of its synaptic contacts with each OFFα (Figure 1F,I; Table S1). A small fraction of AII contacts were made onto OFFα somas, axon initial segments and proximal dendrites passing through the ON layer (Figure 1D,H,G,J; Table S1). OFFαs also received ON/GCL inputs from wide-field ACs (Figure S3). AII arboreal dendrites that did not contact either OFFα GC did not contain presynaptic active zones, even when closely apposed to the somatic regions of other GCs. AII chemical synaptic ON/GCL outputs may, therefore, target OFFα GCs exclusively.

Although most AII outputs in the OFF layer target OFF CBs[14,22], those that contacted GCs exhibited strong preference for OFFαs: 72% of OFF layer AII-GC synapses (from 31 completely traced AIIs) targeted one of the two identified OFFαs (Table S1). As each point in retinal space is covered by roughly two s-OFFαs and two t-OFFαs[26], our analysis likely overlooked many inputs onto OFFα dendrites that could not be identified conclusively because their parent somas were not contained in the dataset. These results corroborate recent physiological observations in guinea pig retina that AIIs contact primarily GC types corresponding to s-OFFαs and t-OFFαs[10].

AIIs made ON/GCL contacts onto OFFαs only when they were located almost directly above an OFFα soma (Figure 1F,G,I,J). Consequently, although many AIIs made OFF layer synapses onto both OFFαs, none made ON/GCL inputs to both (Figure 1F,I). Although we did not reconstruct completely every AII in the dataset, every ON/GCL AII-OFFα synapse was traced back to a fully reconstructed AII; all but one AII making ON/GCL synapses also provided OFF layer input to the same OFFα. AIIs making no ON/GCL synapses exhibited no apparent differences compared to those that did, making similar numbers of OFF layer synapses to the OFFα GCs (Table S1). These similarities suggest that AIIs providing ON/GCL inputs to OFFαs do not represent a distinct AII subtype (see Discussion); rather, this connectivity may depend primarily on proximity of an AII's arboreal dendrites to OFFα somas.

OFFαs express glycine receptors in the GCL and ON layer of the IPL

We next examined glycine receptor (GlyR) expression in OFFαs using fluorescence immunohistochemistry (Figure 2). GlyRs require α subunits to function[27], and OFFαs

express α_1 exclusively[28]. Here, we labeled GCs with an antibody to RBPMS (Figure 2A[29]) and observed somatic GlyRα_1 immunoreactivity (Figure 2B) particularly in a subset of GCs expressing SMI-32 (Figure 2C), a marker for αGCs[30] (Figure 2D).

To examine GlyR expression specifically in OFFαs, individual cells were filled with neurobiotin, then fixed and labeled with antibodies to neurobiotin and GlyRα_1 (Figure 2E-H). As expected, OFFαs robustly expressed GlyRα_1 in the OFF layer of the IPL (Figure 2E,F): s-OFFαs and t-OFFαs exhibited greater GlyRα_1 expression in the OFF layer compared to, for example, ON-OFF direction-selective GCs (DSGCs; n = 3 cells of each type, $p = .02$, Mann-Whitney test; Figure 2G), which express primarily GlyRα_2 and GlyRα_4[31]. s-OFFαs and t-OFFαs also exhibited stronger GlyRα_1 expression than DSGCs in the ON layer ($p = .02$, Mann-Whitney test; Figure 2H), even though DSGC dendrites ramified extensively in this layer (Figure 2G). GlyRα_1 expression was higher in s-OFFαs than in t-OFFαs ($p = .02$, Mann-Whitney test; Figure 2H).

Close apposition of RB inputs and arboreal outputs suggests local input-output relationship

ACs have evolved different strategies to couple synaptic input to output[32]: Some relay synaptic input signals to outputs located ~1 mm away[33-36], whereas others couple input to output within sub-micron synaptic structures[37,38]. With chemical outputs to OFFαs from both arboreal and lobular dendrites, AIIs might integrate inputs within and between subcellular compartments to provide output to the same postsynaptic cell.

To examine the spatial relationship between inputs and output in AIIs, we annotated all RB inputs (n = 139) onto AII arboreal dendrites that contacted the identified t-OFFα and s-OFFα in the ON layer or GCL (Figure 3A) and measured the linear location along the dendrite of each input and output relative to the dendritic terminus (Figure 3B). Most RB inputs were made onto the last 15 μm of AII terminal dendrites (median = 13.1 μm), whereas outputs to OFFαs arose primarily within the last 5 μm (median = 4.7 μm; Figure 3B). Only one output synapse was located within 300 nm of an RB input, however, arguing against hyperlocal input-output coupling. Nonetheless, these results suggested that excitatory inputs from RBs might depolarize the dendritic membrane sufficiently to activate Ca_v channels and elicit release from nearby presynaptic active zones – particularly at dendritic tips, which are depolarized particularly well by excitatory input[39]. Accordingly, an electrotonic model, together with the experimentally measured relationship between AII membrane potential and glycine release[14], predicts that an excitatory conductance in the AII, approximating that of a miniature EPSC[40,41], would depolarize the dendrite sufficiently to evoke release at nearby output synapses (Figure 3C).

L-type Ca_v channels mediate Ca^{2+} influx into AII arboreal dendrites

Glycine release from AII arboreal dendrites likely requires local expression of functional Ca_v channels. Mouse AIIs express $Ca_v1.3$ (L-type) channels, but widefield fluorescence Ca^{2+} imaging methods detected signals primarily in proximal, lobular dendrites[42,43]. Arboreal dendrites are thinner and more diffuse, however, possibly making Ca^{2+} signals more difficult to detect. To revisit this issue, we recorded from AIIs in whole-mount mouse

retina, filled them with Alexa 594 (50 μM) and the Ca^{2+} indicator dye Fluo-5F (150 μM) and imaged dendrites with confocal microscopy (Figure 4). Visual responses were eliminated by blocking glutamatergic synaptic transmission (see STAR Methods). Depolarization applied under voltage clamp elicited Ca^{2+} indicator signals in arboreal and lobular dendrites (Figure 4A,B). Indicator $\Delta F/F_o$ signals increased with the amplitude of the step depolarization, reflecting the voltage dependence of AII L-type currents (Figure 4C[42]). Dendritic $\Delta F/F_o$ signals of varying size exhibited similar voltage-dependence (Figure 4A), suggesting that responses were not distorted by indicator saturation. All step-evoked indicator signals were blocked by the Ca_v1 channel antagonist isradipine (10 μM; Figure 4D,E).

Indicator $\Delta F/F_o$ amplitudes varied widely across neighboring arboreal varicosities (Figure 4A), suggesting that these signals do not reflect passive Ca^{2+} diffusion from more proximal regions of the cell. Accordingly, signals deep in the IPL/GCL were often larger than in more proximal regions of the same dendrites (Figure 4F-I), suggesting that they reflected local Ca^{2+} influx into arboreal dendrites. This relative increase in signal was more prevalent in dendrites that extended into the GCL near large GC somas characteristic of αGCs (Figure 4I): Along AII dendrites close to αGCs, peak $\Delta F/F_o$ in the most distal ROIs was typically greater than in their neighboring, more proximal ROIs (n = 75 dendrites in 4 AIIs, p = .00002, Mann-Whitney test; Figure 4J,L). In two of these four experiments, we recorded from the adjacent αGC, which in both cases exhibited OFF responses to light stimuli (e.g., Figure S4). In AIIs that were not close to an αGC, the most distal dendritic ROI signals were smaller relative to their more proximal neighbors (n = 166 dendrites in 6 AIIs, $p = 10^{-23}$, Mann-Whitney test; Figure 4K,L).

Strongest AII inputs come from cells located directly above OFFα GCs

SBFSEM analysis indicated that AII-OFFα ON/GCL connections occur only when the presynaptic AII is positioned almost directly above the OFFα soma (Figure 1). For example, all ON/GCL AII inputs to the s-OFFα came from AIIs whose somas were located within 33 μm of s-OFFα in retinotopic space (Figure 1F). By contrast, AII inputs in the OFF layer were more evenly distributed: AIIs located within 36 μm of the s-OFFα made a similar number of OFF connections (4.7 ± 2.3 synapses, n = 10) to those AIIs located 36-72 μm away (3.9 ± 2.2 synapses, n = 25, p = .36, t-test). AII OFF connections to t-OFFαs also were evenly distributed across this spatial scale (≤36 μm: 3.4 ± 1.4 synapses, n = 10; 36-72 μm: 2.9 ± 1.5 synapses, n = 25; p = .35, t-test).

These data suggest that AIIs located within 36 μm of an OFFα may provide stronger synaptic input to this cell, provided that ON layer synapses are functional. To test this, we recorded from OFFαs and measured IPSCs elicited by activating single presynaptic AIIs (Figure 5). Mice expressing Cre recombinase under control of the *Neurod6* promoter (*Neurod6*^{Cre}) were crossed with the Ai27 (Gt(ROSA)26Sor) line that expresses channelrhodopsin (ChR2) and tdTomato in a Cre-dependent fashion (Figure 5A). Although the *Neurod6*^{Cre} line expresses Cre in a non-AII narrow field AC[44], crossing it with Ai27 yielded ChR2 and tdTomato expression in AIIs as well, possibly reflecting leaky expression driven by the ROSA26 cassette (Figure 5A [45]). The AC types labeled in this line could be

distinguished morphologically in *z* stacks obtained at the end of the experiment (Figure 5B; see STAR Methods); only cells identified as AIIs were analyzed here.

ChR2 was activated with laser light pulses centered upon individual AII somas, and IPSCs (V_{hold} = +10 mV) were recorded from voltage clamped OFFαs. Excitatory inputs to ON and OFF bipolar cells were blocked pharmacologically (see STAR Methods), eliminating photoresponses to stimuli delivered in a region lacking tdTomato signal (Figure 5B). ChR-mediated responses were largest when the stimulated AII soma was close (in *x*-*y* space) to that of the recorded αGC (Figure 5A,B). In s-OFFαs, stimulating AIIs located within 36 μm in *x*-*y* space evoked responses that were almost twice as large (median = 31.8 pA, n = 15) as those when AIIs were located 36-72 μm away (median = 17.7 pA, n = 16; p = .0013, Mann-Whitney test; Figure 5C). Similar results were observed in t-OFFαs (0-36 μm: median = 32.6 pA, n = 13; 36-72 μm: median = 18.5, n = 11; p = .0040, Mann-Whitney test; Figure 5D). No significant differences in IPSC amplitudes were observed between s-OFFαs and t-OFFαs in either group (0-36 μm: p = .65; 36-72 μm: p = .72, Mann-Whitney test). AII stimulation elicited no responses in s-ONαs (Figure 5E), confirming AII input specificity and blockade of bipolar cell input.

To examine further direct synaptic connections between AIIs and OFFαs, we obtained whole-cell voltage clamp recordings simultaneously from AIIs and s-OFFαs in whole-mount wild-type retina (Figure 5F). Depolarizing voltage steps delivered to the AII evoked large IPSCs in the s-OFFα when the somas of the two cells were located close to one another in *x*-*y* space (Figure 5G,H): Pairs located within 36 μm yielded larger IPSCs (median = 85.9 pA, n = 5) than those located 36-76 μm apart (median = 9.6 pA, n = 5, p = .002, Mann-Whitney test). Together with our anatomical data, these results indicate that AIIs positioned above OFFα somas provide stronger inhibitory input, compared with peripherally located AIIs, to postsynaptic OFFαs.

ON layer inputs convey rod signals near visual threshold

ON/GCL inputs from AIIs may render s-OFFαs particularly sensitive to light stimuli activating just a few AIIs. To test this, we made cell-attached recordings from s-OFFαs and measured spike responses to dim, small (50-μm-diameter spots) light flashes (10 ms; Figure 6A,B). Even stimuli activating just ~60 rods (0.071 R*/rod[46]), significantly decreased the baseline firing rate (by 38.6 ± 16.6%, n = 7, p = .0011, paired *t*-test), and a 20× stronger flash eliminated spiking almost completely (95.4 ± 5.3% reduction; Figure 6B).

The results thus far suggest that ON/GCL synapses from AIIs, despite constituting only ~2% of the inhibitory inputs to OFFαs (Table S1), may contribute substantial light-evoked inhibition to OFFαs. If so, blocking just these inputs would have a significant effect on OFFα light responses. To test this, we attempted to block ON/GCL inputs preferentially by applying the GlyR antagonist strychnine locally in the GCL. We positioned a puffer pipette containing Alexa 594 (50 μM) and strychnine (2-5 μM) near a patched OFFα soma and delivered 300-ms puffs just prior to the light stimulus (Figure 6C-I). We imaged Alexa fluorescence within the pipette, near the recorded s-OFFα soma and in the OFF layer of the IPL (Figure 6D) to measure its dilution at different distances from the pipette and, therefore, estimate the dilution of strychnine relative to its known concentration within the pipette.

During the 100-ms period following the light stimulus, estimated [strychnine] exceeded 1 μM at the GC soma, but in the OFF layer it remained below its IC_{50} for $GlyR\alpha_1$ (36 nM[47]; Figure 6E). Strychnine application elicited a small (though statistically insignificant) increase in baseline firing rate (from 42.9 ± 15.0 Hz to 53.4 ± 20.3 Hz, n = 7 cell-attached recordings, $p = .067$, paired *t*-test), so we calculated the light-evoked reduction in firing rate as a percentage of the pre-stimulus baseline rate. Strychnine reduced this OFF response over a range of flash intensities (Figure 6F,G). In whole-cell recordings, strychnine applied in the GCL reversibly reduced flash-evoked IPSCs by an average of 47% across all stimulus intensities (n = 8; Figure 6H,I), suggesting that ON/GCL inhibitory inputs influence scotopic visual responses in s-OFFαs.

OFFα inhibitory RFs are smaller than their dendritic fields

Synaptic inputs to GCs typically are distributed evenly across the dendritic arbor (Figure S2[48]), so that GC RFs generally reflect dendritic field (DF) dimensions[16,49,50]. RF size typically is measured by delivering light stimuli to different regions of the RF and fitting the spatial distribution of responses with a Gaussian function[51] (but see[52,53]). Strong RF-DF correlations require that synaptic input strength is relatively even across the dendritic arbor. Inhibitory RFs are usually broader than excitatory RFs[54], because the lateral extent of inhibitory connectivity is greater than that of excitatory bipolar cells. Under scotopic conditions, particularly when visual stimuli are delivered from darkness, excitatory inputs to OFFαs are weak and evoked input is predominantly inhibitory[9,12,55,56]. We postulated that OFFα inhibitory RFs would be smaller than their DF if they were dominated by input from central AIIs.

To test this, we recorded light-evoked postsynaptic currents under scotopic conditions from αGCs and measured RF dimensions (Figure 7). Vertical and horizontal bars of light (0.5 R*/rod/s) were presented at different *x* and *y* displacements, respectively and responses in each spatial dimension were fit with a Gaussian function (Figure 7A; see STAR Methods); the resulting space constants (λ_x and λ_y) were averaged together (λ_{RF}). For comparison with anatomical dimensions, RF diameter was calculated from the region over which the function remained >5% of peak ($2\sqrt{3}\cdot\lambda_{RF}$; Figure 7D).

To measure the DF diameter in the same experiments, cells were filled with Alexa 488 during whole-cell recording and imaged after the experiment (Figure 7A, *right*); a convex polygon drawn around the dendritic arbor was used to calculate the average diameter of the DF. In s-ONαs, the excitatory RF diameter was highly correlated with DF diameter ($r = .84$, n = 12, $p = .00059$; Figure 7A,D). s-OFFαs, by contrast, exhibited inhibitory RFs that were narrower than (n = 19, $p = 6\times10^{-9}$, paired *t*-test) and poorly correlated with their DFs ($r = -.11$, $p = .65$; Figure 7B,D). As a result, s-OFFα RF area constituted a smaller fraction of its DF area when compared to s-ONαs ($p = 1.6\times10^{-5}$, Mann-Whitney test). RF dimensions were not altered significantly by TTX (RF diameter in TTX: 95 ± 11% of control, n = 8 OFFαs, $p = 0.19$, paired *t*-test; Figure S5), indicating that RFs measured this way were not influenced by surround inhibition from wide-field, spiking ACs[57]. In separate experiments in which photopic stimulation evoked reliably detected EPSCs, RFs were generally larger than in scotopic conditions; the photopic IPSC RF diameter in OFFαs was similar to the

DF diameter but still smaller than the EPSC RF diameter, whereas in s-ONαs inhibitory and excitatory RFs exhibited similar dimensions (Figure S6).

AII RFs, measured by evoking PSPs with 0.5 R*/rod/s stimuli, were wider than ($p = 4.3\times10^{-7}$, paired *t*-test) and poorly correlated with their DFs ($r = -0.15$, $p = .65$; Figure 7C,D). AII RFs were narrower than s-OFFα RFs ($p = 2.3\times10^{-7}$, *t*-test; Figure 7D), suggesting that s-OFFα inhibitory RFs are inherited from multiple AIIs. The distribution of AII inputs required to generate the s-OFFα inhibitory RF was estimated by deconvolving the average AII RF Gaussian from that of the s-OFFα inhibitory RF (red line, Figure 7E; see STAR Methods). This prediction most closely matched the spatial distribution of ON layer AII→s-OFFα synapses in the EM dataset (black line, Figure 7E), suggesting that perisomatic inputs from AII heavily influence OFFα inhibitory RFs. Accordingly, when we blocked ON/GCL inputs specifically with local strychnine puffs (as in Figure 6), inhibitory RFs recorded in s-OFFαs became broader (131 ± 12% of control, n = 8, $p = 3\times10^{-5}$, paired *t*-test) due primarily to reduced responsivity in the RF center (Figure 7F,G).

Discussion

Our results reveal an unexpected route for visual signals through the rod pathway of the mammalian retina. Anatomical and physiological data show that a small minority of AIIs inhibit the somatic region of OFFαs, conferring high visual sensitivity and small inhibitory RFs. The close proximity of RB inputs to these outputs within AII arboreal dendrites ensures efficient signal transfer from single RBs to OFFαs. This previously unrecognized motif 1) disobeys the laminar segregation of inputs and outputs within narrow-field (NF) ACs mediating “crossover inhibition” in the IPL, 2) generates RFs that are poorly predicted by dendritic dimensions and 3) reveals heterogeneous synaptic organization within a single cell type.

AIIs “cross over” within the ON layer

Segregated ON and OFF signaling in the IPL is a consistent hallmark of vertebrate retinas[58]. ON and OFF bipolar cells provide excitatory input to ON and OFF GCs in the inner and outer IPL, respectively, strongly correlating morphology and physiology[59-62] (but see[63,64]). Wide-field (WF, typically GABAergic) and NF (glycinergic) ACs influence this circuitry in different ways: WFACs typically mediate lateral interactions within IPL strata, conferring surround feedback or feedforward inhibition to bipolar terminals or GC dendrites, respectively[62,65], and also inhibiting other ACs[66]. NFACs relay signals between IPL layers – “crossover” inhibition[67] that can influence feedforward signals locally via “push-pull” interactions with excitation[9,62,68]. NFACs, including AIIs, are thought to reinforce the ON-OFF segregation by providing ON-driven inhibition to the OFF layer, or vice versa[3]. We show here that AIIs contradict this convention, providing powerful feedforward inhibition onto OFFα somas and proximal dendrites in the ON layer.

AII ON/GCL inputs exert a disproportionate influence on OFFα RFs

Consistent with previous reports[48], we found that synaptic inputs to OFFαs are distributed evenly across the dendritic arbor (Figure 1, S2), an arrangement that typically ensures a

close agreement between DF and RF dimensions[69]. Our physiological experiments revealed, however, that AII inputs to the proximal dendrites, soma and axon cause s-OFFα inhibitory RFs to be smaller than expected from the dimensions of the dendritic arbor (Figure 7D). Each AII ON/GCL input synapse could provide a larger inhibitory conductance than AII synapses in the OFF layer, and/or ON/GCL inputs could exert more influence by virtue of their electrotonic proximity to the soma. We favor the latter mechanism, which likely accentuates the impact of ON/GCL inputs on light-evoked changes in spiking.

Does the mouse retina contain multiple AII subtypes?

In the retina, physiological and molecular classifications of bipolar and ganglion cell types agree remarkably well[61,62,70-72], and cells of one type exhibit consistent connectivity patterns with other cell types[73]. One previous study divided AIIs into two subtypes based on visual sensitivity[74], but two observations suggest that the different AIIs described here do not correspond to those proposed subtypes. First, our EM observations provided no evidence that ON/GCL-projecting AIIs would exhibit distinct light sensitivity: AIIs making ON/GCL synapses received similar RB input compared to those that did not. Second, whereas the previously proposed subtypes constituted roughly equal parts (55%/45%) of the AII population[74], only 11% (14/127) of the AIIs studied in the SBFSEM dataset made ON/GCL chemical synapses.

Reliable connectivity between cell types requires that their processes overlap in space and, in many cases, that cells express specific cell-adhesion molecules[75,76]. AII arborial dendrites appear to target OFFα somas selectively amidst many other options, suggesting that molecular cell-cell interactions may dictate specific connectivity. A distinct subtype of AIIs may express a particular adhesion molecule recognized by OFFαs; alternatively, AIIs could be molecularly homogeneous but only those located above OFFα somas are afforded the geometric opportunity to make ON/GCL contacts. AIIs appear to constitute a single cell type with respect to gene transcription[77], favoring the second possibility.

Relevance to visual signaling in OFFαs

The circuit features described here may underlie the high sensitivity of OFF GCs[78], but specific roles for this pathway in night vision remain to be determined. A recent report suggests that some visually guided behaviors in scotopic conditions rely primarily on ON pathway signals[7]. ONαs receive convergent input from ~10,000 rods[4,79], likely conferring sensivity to low spatial frequencies and ambient luminance. The OFF pathway that we describe gives rise to smaller RFs that may confer greater sensitivity to high-frequency scotopic signals (e.g., edges, stars). These distinct pathways may provide complementary visual information required for fundamentally asymmetric signaling tasks in the ON and OFF pathway when photons are scarce[80].

STAR Methods

RESOURCE AVAILABILITY

Lead contact—Further information and requests for resources should be directed to and will be fulfilled by the lead contact, Jeffrey Diamond (diamondj@ninds.nih.gov).

Materials Availability—This study did not generate new unique reagents.

Data and code availability—All data reported in this paper, as well as any additional information required for its analysis, are available from the lead contact upon request. This study did not report original code.

EXPERIMENTAL MODEL AND SUBJECT DETAILS

All experiments were performed in accordance with protocols approved by the NINDS Animal Care and Use Committee (ASP-1344). Mice (either sex) were maintained on a 12:12 light-dark cycle and provided free access to food and water. Prior to electrophysiological experiments or immunohistochemistry, mice were deeply anaesthetized with isoflurane (Baxter) and euthanized via decapitation.

METHOD DETAILS

SBFSEM Analysis—A 3D SBFSEM dataset (k0725) of a 50×210×260 μm^3 block of P30 C57BL/6 mouse retina (13.2×13.2×26 nm^3 voxels[24]) was analyzed as described previously[14,57]. AIIs were identified based on morphological characteristics and synaptic input from RBs. RB inputs were distinguished by their location deep in the IPL and presynaptic ribbons that are larger than those in CB terminals[6,14]. The s-OFFα and t-OFFα were identified by soma diameter and dendritic ramification in the distal IPL. Skeletonization and annotation were performed manually using Knossos[82]. Voxel coordinates were tilt-corrected and normalized either to the positions of the ON and OFF SACs[24]. Soma diameter was determined by tracing the soma perimeter with a convex polygon, calculating the area and then the average diameter (i.e., the diameter of a circle of the same area).

Immunohistochemistry (Figure 2A-D)—Whole retinas were dissected from C57BL6-WT mice (~P60) and fixed in 4% paraformaldehyde (PFA) in 0.1M phosphate buffer solution (PBS) for 20 min at room temperature (RT), then rinsed with PBS. Retinas were pre-incubated for 5 h at RT or overnight at 4°C in blocking solution containing 10% donkey serum (Sigma, MO), 2% BSA, 0.5% Triton X-100 and 0.1% sodium azide in PBS. Retinas were then incubated for three nights at 4°C with primary antibodies against RBPMS (guinea pig polyclonal, 1:500; Phosphosolution), $GlyR\alpha_1$ (rabbit monoclonal, 1:500; Synaptic Systems) and SMI32 (mouse monoclonal, 1:500; Millipore-Sigma) in blocking solution. Retinas were then rinsed 3 times in PBS, incubated overnight at 4°C with secondary antibodies against guinea pig (donkey, Alexa Fluor 488, 1:500; Invitrogen), rabbit (donkey, Cy3, 1:500; Jackson ImmunoResearch) and mouse (donkey, Cy5, 1:500; Jackson ImmunoResearch) in blocking buffer, rinsed in PBS and thereafter mounted with DAPI mounting medium (Vector Labs). Immunoreactivity was imaged using a confocal microscope (Zeiss LSM 580, 20×/1.0NA objective).

Single-cell immunolabeling (Figure 2E-H)—GCs in whole-mount retinas were filled with 4% Neurobiotin through a whole-cell patch electrode, then fixed for 15 mins at RT in artificial cerebrospinal fluid containing 4% paraformaldehyde. Post-fixation, retinas were washed in 0.1M PBS, pre-incubated overnight at 4°C in blocking solution containing 5%

donkey serum and 0.5% Triton in PBS and then incubated for 3 nights at 4°C with primary antibody against GlyRα_1 (mouse monoclonal mAb2b, 1:500; Synaptic Systems) in blocking solution. Retinas were subsequently rinsed in PBS, incubated with a secondary antibody against mouse (goat anti-mouse 488, 1:000; Invitrogen) and streptavidin conjugated to Alexa Fluor 568 (1:1000; Invitrogen), rinsed in PBS and mounted using Vectashield anti-fade mounting medium (Vector labs).

Images were acquired using a confocal microscope (Leica SP8, 63×/1.4NA objective). Image stacks encompassing the entire GC (soma and dendritic arbor) were acquired, median-filtered in FIJI (NIH) and visualized with Amira software (Thermo Fisher Scientific). Individual GCs were masked in 3D via the *LabelField* function in Amira. Once a GC was isolated in a 3D mask, the GlyRα_1 receptor channel was multiplied with the GC mask to isolate the GlyRα_1 signal within the GC. For quantification of the GlyRα_1 signal within the ON (soma and dendritic arbor within the ON lamina) and OFF (dendritic arbor within the OFF lamina) arbors of the GC, the volume of GlyRα_1 signal within the RGC compartment and above background (threshold of 3 standard deviations above the noise peak applied to eliminate background pixels) was estimated and normalized to the GC compartment volume (see also [83]).

NEURON Modeling—A compartmental model (NEURON simulation software[84]) comprised a soma (20 μm diameter, 1 compartment) connected to a dendrite (100 μm long, 0.5 μm diameter, 10 compartments; Figure 3C). Membrane capacitance, resistance and resting potential were 1 μF·cm^{-2}, 100 μS·cm^{-2} and −60 mV, respectively; axial resistance was 100 Ω·cm. Gap junctions in arboreal dendrites may offer alternative conduction pathways, but most are located closer to the soma[2,6] and were neglected in this simplified simulation. An excitatory synaptic conductance (E_{rev} = 0 mV), introduced at different points along the dendrite (see Figure 3C), was represented as:

$$g_{syn} = g_{max}\left(\frac{t}{\tau}\right)e^{-\frac{t}{\tau}}$$

where g_{max} = 250 pS and τ = 2 ms.

Live tissue preparation and electrophysiology—Eyes were removed from adult mice (P30-80) of either sex and retinas were isolated at room temperature (ChR2 and Ca^{2+} imaging experiments) or 32-34°C (scotopic RF measurements and somatic puff experiments) in bicarbonate-buffered Ames media (Sigma) equilibrated with carbogen (95% O_2/5% CO_2). Tissue was trimmed and mounted GCL up (i.e. whole-mount), placed under a two-photon laser-scanning microscope (Zeiss 510 or Scientifica Hyperscope) and superfused during experiments with Ames (which contains 1.1 mM Ca and 1.2 mM Mg) at 30-34°C (4-8 mL/min). For experiments examining retinal signaling in response to visual stimuli, mice were dark adapted for >2 hrs prior to dissection and retinas were isolated under infrared illumination (940 nm LED light source, Thorlabs). Retinas used for Ca^{2+} imaging experiments were isolated under dim red light. Cells within the whole-mount retina were selected for recording under differential interference contrast (DIC) optics (940 nm): αGCs were identified by their large soma size, and AIIs by their pear-shaped somas that jut into

the IPL from the INL. To access the cells for recording, a small hole was torn in the inner limiting membrane with a patch pipette, which was then replaced with a second pipette for recording.

Cell-attached and whole-cell recordings were made with an electronic amplifier (MultiClamp 700B, Molecular Devices) controlled with custom software written in IgorPro or Matlab (Symphony: https://symphony-das.github.io). Patch electrodes (1.5mm OD borosilicate glass, 4-5 MΩ for GCs, 5.5-6.5 MΩ for AIIs) were filled with internal solution (280-285 mOsm, pH 7.4) containing (mM): 90 $CsCH_3SO_3$ or KCH_3SO_3, 20 TEA-Cl, 4 MgATP, 0.4 NaGTP, 10 EGTA, 10 Na_2 Phosphocreatine, 10 HEPES.

Ca^{2+} indicator imaging—Ca^{2+} indicator imaging experiments were performed on a Zeiss (Thornwood, NY) LSM-510 confocal microscope (40x/1.0 DIC W Plan-Apochromat objective) controlled by ZEN 2009 software and custom macros (Igor Pro, WaveMetrics, Lake Oswego, OR). AIIs were patched in whole mounts and filled with a Cs^+-based intracellular solution containing Alexa 594 hydrazide (50 μM; Thermo Fisher Scientific) to visualize cell morphology and the Ca^{2+} indicator Fluo-5F (150 μM; Thermo Fisher Scientific). No additional intracellular Ca^{2+} buffers were present during imaging experiments. Imaging commenced 10-15 minutes after establishing whole-cell recordings to allow dyes to diffuse throughout the cell. Alexa 594 and Fluo-5F were excited by 543-nm He-Ne and 488-nm Ar lasers. Transient indicator signals were evoked by 100 ms voltage steps applied through the recording pipette every 15-20 seconds, measured in (bidirectional) frame scan mode (10.4 Hz) and low-pass filtered (2-5 Hz) offline. Glutamatergic transmission and light responses were routinely blocked pharmacologically by DNQX (20 μM; Abcam), R-CPP (5 μM; Tocris Bioscience) and L-AP4 (20 μM, Abcam) before imaging started. Image analysis was performed using custom macros in IgorPro. Individual lobular and arboreal varicosities were analyzed as single regions of interest (ROIs) and all data are presented as ΔF/F. *Z*-stacks (1 μm intervals, 4 images averaged at each *z* level) were acquired at the end of each experiment to reconstruct cell morphology.

Optogenetic stimulation—Optogenetic stimulation experiments were performed on Zeiss LSM-510 (40×/1.0 NA objective) and a Nikon C1 (40×/0.8 NA objective). *Neurod6*^{Cre}and Ai27 (Gt(ROSA)26Sor) lines were crossed to yield mice that expressed ChR2 and tdTomato in AIIs and at least one other narrow-field AC type. AIIs were distinguished from other labelled amacrines due to their stronger tdTomato expression and their arboreal dendrites that extended through the entirety of the IPL and sometimes into the GCL (the dendrites of other labelled ACs were constrained to IPL sublaminas 1-4). ChR2 was activated with a 500 ms spot scan from a 488 nm Ar laser centered over an AC soma. Stimulation timing was verified by diverting a fraction of the laser light to a photodiode. ChR2-evoked IPSCs were recorded from GCs in whole-cell voltage clamp (V_{hold} = +10 mV) with a Cs-based internal solution supplemented with Alexa488 (50 uM). Photoreceptor-driven light responses to the 488 nm laser were eliminated by blocking all glutamatergic synaptic transmission in the retina (e.g. eliminating bipolar transmission) with L-AP4 (20 μM; Abcam), UBP 310 (25 μM; Abcam), NBQX/DNQX (10 μM/20 μM; Abcam) and D-AP5/R-CPP (25 μM/5 μM; Tocris Bioscience). AII-GC distance was

determined by collecting a composite *z*-stack and measuring the linear distance between the centers of the AII (red) and GC (yellow) somas in the *x*-*y* plane.

Visual stimulation—Visual stimuli were controlled by Symphony, generated with a customized DMD projector (4500 Light Crafter, Texas Instruments[85]) and a 405 nm LED (Thorlabs), attenuated by neutral density filters (~6 log units) and routed through the microscope condenser, which was adjusted so that images were in focus at the level of the rod outer segments. Spectral and power densities were measured at the sample plane and converted to R*/rod/s as previously described[86]. Scotopic RFs of AII amacrine cells and GCs were probed with 50 × 500 μm^2 bars (250 ms) that elicited 0.1-1 R*/rod. Excitatory RFs of s-ONα s and AIIs were probed at 50 and 25 μm intervals, respectively; inhibitory RFs in s-OFFα s were probed at 25 μm intervals. Responses to bars at each location were averaged and baseline subtracted prior to measuring amplitude by averaging over a window 100-350 ms following stimulus onset. Bars were presented 5-10 times at each location and in two orthogonal directions (i.e., 0° and 90°). In some photopic experiments, responses were obtained with bars oriented at 0°, 36°, 72°, 108° and 144°. In these cases, responses to 72° and 108° bars were averaged together to approximate the 90° case, then averaged together with the 0° data. Response amplitudes were plotted versus bar position and fit by a sum of two Gaussians (one for the center and a second, larger one of opposite polarity for the surround). Surround amplitudes typically were small relative to those in the center.

Puff application of strychnine—Contributions from somatic glycine receptors were examined by locally puffing strychnine onto the GC soma while recording responses to small (50 μm diameter) spots (17 ms flash) positioned in the center of the GC's RF. Puff pipettes (6-8 MΩ) were filled with 2-10 uM strychnine (to block glycine receptors) and 50 uM Alexa594 (to monitor the diffusion of the puff and estimate strychnine concentration over space and time). Small holes were torn into the inner limiting membrane on either side of the GC somas to create room for the pipettes. This step required particular care to ensure that synaptic connections in the GCL remained intact. Puffs were applied (Picospritzer, Parker; ~3 PSI) for 300 ms prior to the flash; trials were repeated at 5-6 s intervals. Flashes of four different intensities were presented, and average responses (5-7 trials) were obtained for each flash strength in each condition (control, puff, wash). Data from the first 8 flashes in each condition were excluded from further analysis to allow for adaptation to the mechanical puff. Average responses were smoothed (10 ms box filter) prior to measuring minimum spike rate or maximum INH current. Spike suppression was calculated by dividing response minimums by the baseline firing rate. Strychnine concentrations were estimated by measuring average Alexa594 fluorescence within a ~15 um^2 ROI and normalizing this to the maximum fluorescence signal (near the pipette tip or within the pipette).

Estimating the distribution of AII inputs from RF dimensions (Figure 7E)—Under scotopic conditions, the spatial dimensions of the s-OFFα inhibitory RF can be expressed as the convolution of a function describing the average AII RF with a function describing the spatial distribution of AII inputs onto the s-OFFα (weighted by the relative strength of the inputs across space). Both the s-OFFα and AII RFs are well described by Gaussian functions (Figure 7), so the weighted distribution of AII inputs also should be

well described by a Gaussian function. This distribution was estimated by deconvolving the average AII RF Gaussian from the s-OFFα inhibitory RF Gaussian (Figure 7E). As the variances of Gaussian distributions add under convolution, the space constant of a Gaussian describing the weighted AII input distribution ($\lambda_{\text{AII inputs}}$) can be calculated from the space constants of the other two Gaussian functions ($\lambda_{\text{AII RF}}$ and $\lambda_{\text{s-OFFα RF}}$):

$$\lambda_{AII\ inputs} = \sqrt{\lambda_{s-OFF\alpha\ RF}^2 - \lambda_{AII\ RF}^2}$$

QUANTIFICATION AND STATISTICAL ANALYSIS

All statistical analysis was performed using Igor Pro. Reported n values indicate number of cells. Except where noted, normally distributed (as determined by the Jarque-Bera test) group data values are reported as mean ± SD and compared with a *t*-test. Otherwise, data are compared with a Wilcoxon rank test. Pearson's correlation coefficient (r) and correlation significance was calculated with a one-tailed linear correlation test (Igor Pro). Significant differences were concluded if $p < .05$.

Supplementary Material

Refer to Web version on PubMed Central for supplementary material.

Acknowledgments

This work was supported by the NINDS Intramural Research Program (NS003039 to JSD), the NEI (EY017836 to JHS, EY028111 to FR) and an unrestricted grant from Research to Prevent Blindness, Inc. to UW Madison Department of Ophthalmology and Visual Sciences (MH).

References

1. Demb JB and Singer JH (2012). Intrinsic properties and functional circuitry of the AII amacrine cell. Vis Neurosci 29, 51–60. [PubMed: 22310372]
2. Marc RE, Anderson JR, Jones BW, Sigulinsky CL and Lauritzen JS (2014). The AII amacrine cell connectome: a dense network hub. Front Neural Circuits 8, 104. [PubMed: 25237297]
3. Famiglietti EV Jr. and Kolb H (1975). A bistratified amacrine cell and synaptic cirucitry in the inner plexiform layer of the retina. Brain Res 84, 293–300. [PubMed: 1111833]
4. Tsukamoto Y, Morigiwa K, Ueda M and Sterling P (2001). Microcircuits for night vision in mouse retina. J Neurosci 21, 8616–23. [PubMed: 11606649]
5. Pourcho RG and Goebel DJ (1985). A combined Golgi and autoradiographic study of (3H)glycine-accumulating amacrine cells in the cat retina. J Comp Neurol 233, 473–80. [PubMed: 2984258]
6. Strettoi E, Raviola E and Dacheux RF (1992). Synaptic connections of the narrow-field, bistratified rod amacrine cell (AII) in the rabbit retina. J Comp Neurol 325, 152–68. [PubMed: 1460111]
7. Smeds L, Takeshita D, Turunen T, Tiihonen J, Westo J, Martyniuk N, Seppanen A and Ala-Laurila P (2019). Paradoxical Rules of Spike Train Decoding Revealed at the Sensitivity Limit of Vision. Neuron 104, 576–587 e11. [PubMed: 31519460]
8. Arman AC and Sampath AP (2012). Dark-adapted response threshold of OFF ganglion cells is not set by OFF bipolar cells in the mouse retina. J Neurophysiol 107, 2649–59. [PubMed: 22338022]
9. van Wyk M, Wassle H and Taylor WR (2009). Receptive field properties of ON- and OFF-ganglion cells in the mouse retina. Vis Neurosci 26, 297–308. [PubMed: 19602302]
10. Beaudoin DL, Kupershtok M and Demb JB (2019). Selective synaptic connections in the retinal pathway for night vision. J Comp Neurol 527, 117–132. [PubMed: 28856684]

11. Manookin MB, Beaudoin DL, Ernst ZR, Flagel LJ and Demb JB (2008). Disinhibition combines with excitation to extend the operating range of the OFF visual pathway in daylight. J Neurosci 28, 4136–50. [PubMed: 18417693]
12. Murphy GJ and Rieke F (2008). Signals and noise in an inhibitory interneuron diverge to control activity in nearby retinal ganglion cells. Nat Neurosci 11, 318–26. [PubMed: 18223648]
13. Münch TA, da Silveira RA, Siegert S, Viney TJ, Awatramani GB and Roska B (2009). Approach sensitivity in the retina processed by a multifunctional neural circuit. Nat Neurosci 12, 1308–16. [PubMed: 19734895]
14. Graydon CW, Lieberman EE, Rho N, Briggman KL, Singer JH and Diamond JS (2018). Synaptic Transfer between Rod and Cone Pathways Mediated by AII Amacrine Cells in the Mouse Retina. Curr Biol 28, 2739–2751 e3. [PubMed: 30122532]
15. Peichl L, Ott H and Boycott BB (1987). Alpha ganglion cells in mammalian retinae. Proc R Soc Lond B Biol Sci 231, 169–97. [PubMed: 2889210]
16. Boycott BB and Wassle H (1974). The morphological types of ganglion cells of the domestic cat's retina. J Physiol 240, 397–419. [PubMed: 4422168]
17. Dhande OS, Stafford BK, Lim JA and Huberman AD (2015). Contributions of Retinal Ganglion Cells to Subcortical Visual Processing and Behaviors. Annu Rev Vis Sci 1, 291–328. [PubMed: 28532372]
18. Cleland BG and Levick WR (1974). Brisk and sluggish concentrically organized ganglion cells in the cat's retina. J Physiol 240, 421–56. [PubMed: 4421622]
19. Krieger B, Qiao M, Rousso DL, Sanes JR and Meister M (2017). Four alpha ganglion cell types in mouse retina: Function, structure, and molecular signatures. PLoS One 12, e0180091. [PubMed: 28753612]
20. Dacheux RF and Raviola E (1986). The rod pathway in the rabbit retina: a depolarizing bipolar and amacrine cell. J Neurosci 6, 331–45. [PubMed: 3950701]
21. Mills SL and Massey SC (1995). Differential properties of two gap junctional pathways made by AII amacrine cells. Nature 377, 734–7. [PubMed: 7477263]
22. Tsukamoto Y and Omi N (2013). Functional allocation of synaptic contacts in microcircuits from rods via rod bipolar to AII amacrine cells in the mouse retina. J Comp Neurol 521, 3541–55. [PubMed: 23749582]
23. Zandt BJ, Liu JH, Veruki ML and Hartveit E (2017). AII amacrine cells: quantitative reconstruction and morphometric analysis of electrophysiologically identified cells in live rat retinal slices imaged with multi-photon excitation microscopy. Brain Struct Funct 222, 151–182. [PubMed: 26951289]
24. Ding H, Smith RG, Poleg-Polsky A, Diamond JS and Briggman KL (2016). Species-specific wiring for direction selectivity in the mammalian retina. Nature 535, 105–10. [PubMed: 27350241]
25. Roy S, Jun NY, Davis EL, Pearson J and Field GD (2021). Inter-mosaic coordination of retinal receptive fields. Nature.
26. Bae JA, Mu S, Kim JS, Turner NL, Tartavull I, Kemnitz N, Jordan CS, Norton AD, Silversmith WM, Prentki R, Sorek M, David C, Jones DL, Bland D, Sterling ALR, Park J, Briggman KL, Seung HS and Eyewirers (2018). Digital Museum of Retinal Ganglion Cells with Dense Anatomy and Physiology. Cell 173, 1293–1306 e19. [PubMed: 29775596]
27. Betz H and Laube B (2006). Glycine receptors: recent insights into their structural organization and functional diversity. J Neurochem 97, 1600–10. [PubMed: 16805771]
28. Majumdar S, Heinze L, Haverkamp S, Ivanova E and Wassle H (2007). Glycine receptors of A-type ganglion cells of the mouse retina. Vis Neurosci 24, 471–87. [PubMed: 17550639]
29. Rodriguez AR, de Sevilla Muller LP and Brecha NC (2014). The RNA binding protein RBPMS is a selective marker of ganglion cells in the mammalian retina. J Comp Neurol 522, 1411–43. [PubMed: 24318667]
30. Lin B, Wang SW and Masland RH (2004). Retinal ganglion cell type, size, and spacing can be specified independent of homotypic dendritic contacts. Neuron 43, 475–85. [PubMed: 15312647]
31. Pyle IS (2019). Glycine receptor expression across identified retinal ganglion cell types. In Electronic Theses and Dissertations, p. 3187.

32. Diamond JS (2017). Inhibitory Interneurons in the Retina: Types, Circuitry, and Function. Annu Rev Vis Sci 3, 1–24. [PubMed: 28617659]
33. Bloomfield SA and Völgyi B (2007). Response properties of a unique subtype of wide-field amacrine cell in the rabbit retina. Vis Neurosci 24, 459–69. [PubMed: 17900375]
34. Greschner M, Field GD, Li PH, Schiff ML, Gauthier JL, Ahn D, Sher A, Litke AM and Chichilnisky EJ (2014). A polyaxonal amacrine cell population in the primate retina. J Neurosci 34, 3597–606. [PubMed: 24599459]
35. Dacey DM (1989). Axon-bearing amacrine cells of the macaque monkey retina. J Comp Neurol 284, 275–93. [PubMed: 2754037]
36. Manookin MB, Puller C, Rieke F, Neitz J and Neitz M (2015). Distinctive receptive field and physiological properties of a wide-field amacrine cell in the macaque monkey retina. J Neurophysiol 114, 1606–16. [PubMed: 26133804]
37. Chávez AE, Singer JH and Diamond JS (2006). Fast neurotransmitter release triggered by Ca influx through AMPA-type glutamate receptors. Nature 443, 705–8. [PubMed: 17036006]
38. Grimes WN, Zhang J, Tian H, Graydon CW, Hoon M, Rieke F and Diamond JS (2015). Complex inhibitory microcircuitry regulates retinal signaling near visual threshold. J Neurophysiol 114, 341–53. [PubMed: 25972578]
39. Rall W (1969). Time constants and electrotonic length of membrane cylinders and neurons. Biophys J 9, 1483–508. [PubMed: 5352228]
40. Singer JH, Lassova L, Vardi N and Diamond JS (2004). Coordinated multivesicular release at a mammalian ribbon synapse. Nat Neurosci 7, 826–33. [PubMed: 15235608]
41. Jarsky T, Tian M and Singer JH (2010). Nanodomain control of exocytosis is responsible for the signaling capability of a retinal ribbon synapse. J Neurosci 30, 11885–95. [PubMed: 20826653]
42. Habermann CJ, O'Brien BJ, Wassle H and Protti DA (2003). AII amacrine cells express L-type calcium channels at their output synapses. J Neurosci 23, 6904–13. [PubMed: 12890785]
43. Balakrishnan V, Puthussery T, Kim MH, Taylor WR and von Gersdorff H (2015). Synaptic Vesicle Exocytosis at the Dendritic Lobules of an Inhibitory Interneuron in the Mammalian Retina. Neuron 87, 563–75. [PubMed: 26247863]
44. Kay JN, Voinescu PE, Chu MW and Sanes JR (2011). Neurod6 expression defines new retinal amacrine cell subtypes and regulates their fate. Nature Neuroscience 14, 965–U45. [PubMed: 21743471]
45. Prabhakar A, Vujovic D, Cui L, Olson W and Luo W (2019). Leaky expression of channelrhodopsin-2 (ChR2) in Ai32 mouse lines. PLoS One 14, e0213326. [PubMed: 30913225]
46. Jeon CJ, Strettoi E and Masland RH (1998). The major cell populations of the mouse retina. J Neurosci 18, 8936–46. [PubMed: 9786999]
47. Grudzinska J, Schemm R, Haeger S, Nicke A, Schmalzing G, Betz H and Laube B (2005). The beta subunit determines the ligand binding properties of synaptic glycine receptors. Neuron 45, 727–39. [PubMed: 15748848]
48. Bleckert A, Parker ED, Kang Y, Pancaroglu R, Soto F, Lewis R, Craig AM and Wong RO (2013). Spatial relationships between GABAergic and glutamatergic synapses on the dendrites of distinct types of mouse retinal ganglion cells across development. PLoS One 8, e69612. [PubMed: 23922756]
49. Cleland BG, Levick WR and Wassle H (1975). Physiological identification of a morphological class of cat retinal ganglion cells. J Physiol 248, 151–71. [PubMed: 1151804]
50. Brown JE and Major D (1966). Cat retinal ganglion cell dendritic fields. Exp Neurol 15, 70–8. [PubMed: 5934665]
51. Enroth-Cugell C, Robson JG, Schweitzer-Tong DE and Watson AB (1983). Spatio-temporal interactions in cat retinal ganglion cells showing linear spatial summation. J Physiol 341, 279–307. [PubMed: 6620181]
52. Rhoades CE, Shah NP, Manookin MB, Brackbill N, Kling A, Goetz G, Sher A, Litke AM and Chichilnisky EJ (2019). Unusual Physiological Properties of Smooth Monostratified Ganglion Cell Types in Primate Retina. Neuron.

53. Ran Y, Huang Z, Baden T, Schubert T, Baayen H, Berens P, Franke K and Euler T (2020). Type-specific dendritic integration in mouse retinal ganglion cells. Nat Commun 11, 2101. [PubMed: 32355170]
54. Kuffler SW (1953). Discharge patterns and functional organization of mammalian retina. J Neurophysiol 16, 37–68. [PubMed: 13035466]
55. Murphy GJ and Rieke F (2006). Network variability limits stimulus-evoked spike timing precision in retinal ganglion cells. Neuron 52, 511–24. [PubMed: 17088216]
56. Margolis DJ and Detwiler PB (2007). Different mechanisms generate maintained activity in ON and OFF retinal ganglion cells. J Neurosci 27, 5994–6005. [PubMed: 17537971]
57. Park SJ, Lieberman EE, Ke JB, Rho N, Ghorbani P, Rahmani P, Jun NY, Lee HL, Kim IJ, Briggman KL, Demb JB and Singer JH (2020). Connectomic analysis reveals an interneuron with an integral role in the retinal circuit for night vision. Elife 9.
58. Famiglietti EV Jr. and Kolb H (1976). Structural basis for ON-and OFF-center responses in retinal ganglion cells. Science 194, 193–5. [PubMed: 959847]
59. Wässle H, Puller C, Müller F and Haverkamp S (2009). Cone contacts, mosaics, and territories of bipolar cells in the mouse retina. J Neurosci 29, 106–17. [PubMed: 19129389]
60. Wu SM, Gao F and Maple BR (2000). Functional architecture of synapses in the inner retina: segregation of visual signals by stratification of bipolar cell axon terminals. J Neurosci 20, 4462–70. [PubMed: 10844015]
61. Baden T, Berens P, Franke K, Roman Roson M, Bethge M and Euler T (2016). The functional diversity of retinal ganglion cells in the mouse. Nature 529, 345–50. [PubMed: 26735013]
62. Franke K, Berens P, Schubert T, Bethge M, Euler T and Baden T (2017). Inhibition decorrelates visual feature representations in the inner retina. Nature 542, 439–444. [PubMed: 28178238]
63. Zhang DQ, Zhou TR and McMahon DG (2007). Functional heterogeneity of retinal dopaminergic neurons underlying their multiple roles in vision. J Neurosci 27, 692–9. [PubMed: 17234601]
64. Hoshi H, Liu WL, Massey SC and Mills SL (2009). ON inputs to the OFF layer: bipolar cells that break the stratification rules of the retina. J Neurosci 29, 8875–83. [PubMed: 19605625]
65. Vaney DI (1990). The mosaic of amacrine cells in the mammalian retina. Prog. Ret. Res. 9, 49–100.
66. Eggers ED and Lukasiewicz PD (2010). Interneuron circuits tune inhibition in retinal bipolar cells. J Neurophysiol 103, 25–37. [PubMed: 19906884]
67. Roska B and Werblin F (2001). Vertical interactions across ten parallel, stacked representations in the mammalian retina. Nature 410, 583–587. [PubMed: 11279496]
68. McGuire BA, Stevens JK and Sterling P (1984). Microcircuitry of bipolar cells in cat retina. J Neurosci 4, 2920–38. [PubMed: 6502212]
69. Yang G and Masland RH (1994). Receptive fields and dendritic structure of directionally selective retinal ganglion cells. J Neurosci 14, 5267–80. [PubMed: 8083735]
70. Laboissonniere LA, Goetz JJ, Martin GM, Bi R, Lund TJS, Ellson L, Lynch MR, Mooney B, Wickham H, Liu P, Schwartz GW and Trimarchi JM (2019). Molecular signatures of retinal ganglion cells revealed through single cell profiling. Sci Rep 9, 15778. [PubMed: 31673015]
71. Shekhar K, Lapan SW, Whitney IE, Tran NM, Macosko EZ, Kowalczyk M, Adiconis X, Levin JZ, Nemesh J, Goldman M, McCarroll SA, Cepko CL, Regev A and Sanes JR (2016). Comprehensive Classification of Retinal Bipolar Neurons by Single-Cell Transcriptomics. Cell 166, 1308–1323 e30. [PubMed: 27565351]
72. Tran NM, Shekhar K, Whitney IE, Jacobi A, Benhar I, Hong G, Yan W, Adiconis X, Arnold ME, Lee JM, Levin JZ, Lin D, Wang C, Lieber CM, Regev A, He Z and Sanes JR (2019). Single-Cell Profiles of Retinal Ganglion Cells Differing in Resilience to Injury Reveal Neuroprotective Genes. Neuron 104, 1039–1055 e12. [PubMed: 31784286]
73. Helmstaedter M, Briggman KL, Turaga SC, Jain V, Seung HS and Denk W (2013). Connectomic reconstruction of the inner plexiform layer in the mouse retina. Nature 500, 168–74. [PubMed: 23925239]
74. Pang JJ, Gao F and Wu SM (2012). Physiological characterization and functional heterogeneity of narrow-field mammalian amacrine cells. J Physiol 590, 223–34. [PubMed: 22083601]

75. Yamagata M, Weiner JA and Sanes JR (2002). Sidekicks: synaptic adhesion molecules that promote lamina-specific connectivity in the retina. Cell 110, 649–60. [PubMed: 12230981]
76. Hynes RO and Lander AD (1992). Contact and adhesive specificities in the associations, migrations, and targeting of cells and axons. Cell 68, 303–22. [PubMed: 1733501]
77. Yan W, Laboulaye MA, Tran NM, Whitney IE, Benhar I and Sanes JR (2020). Mouse Retinal Cell Atlas: Molecular Identification of over Sixty Amacrine Cell Types. J Neurosci 40, 5177–5195. [PubMed: 32457074]
78. Ala-Laurila P and Rieke F (2014). Coincidence detection of single-photon responses in the inner retina at the sensitivity limit of vision. Curr Biol 24, 2888–98. [PubMed: 25454583]
79. Dunn FA, Doan T, Sampath AP and Rieke F (2006). Controlling the gain of rod-mediated signals in the Mammalian retina. J Neurosci 26, 3959–70. [PubMed: 16611812]
80. Pandarinath C, Victor JD and Nirenberg S (2010). Symmetry breakdown in the ON and OFF pathways of the retina at night: functional implications. J Neurosci 30, 10006–14. [PubMed: 20668185]
81. Vaney DI, Gynther IC and Young HM (1991). Rod-signal interneurons in the rabbit retina: 2. AII amacrine cells. J Comp Neurol 310, 154–69. [PubMed: 1955580]
82. Helmstaedter M, Briggman KL and Denk W (2011). High-accuracy neurite reconstruction for high-throughput neuroanatomy. Nat Neurosci 14, 1081–8. [PubMed: 21743472]
83. Hoon M, Sinha R and Okawa H (2017). Using Fluorescent Markers to Estimate Synaptic Connectivity In Situ. Methods Mol Biol 1538, 293–320. [PubMed: 27943198]
84. Carnevale NT and Hines ML (2006). The NEURON Book (Cambridge, UK: Cambridge University Press).
85. Franke K, Maia Chagas A, Zhao Z, Zimmermann MJ, Bartel P, Qiu Y, Szatko KP, Baden T and Euler T (2019). An arbitrary-spectrum spatial visual stimulator for vision research. Elife 8.
86. Grimes WN, Hoon M, Briggman KL, Wong RO and Rieke F (2014). Cross-synaptic synchrony and transmission of signal and noise across the mouse retina. Elife 3, e03892. [PubMed: 25180102]

Highlights

- AII amacrine cells make dendrosomatic synapses exclusively onto OFFα ganglion cells.
- Only AIIs located directly above OFFα ganglion cells make dendrosomatic contacts.
- AII dendrites express voltage-gated calcium influx near synaptic outputs.
- AII dendrosomatic inputs render OFFαs highly sensitive to narrow visual stimuli.

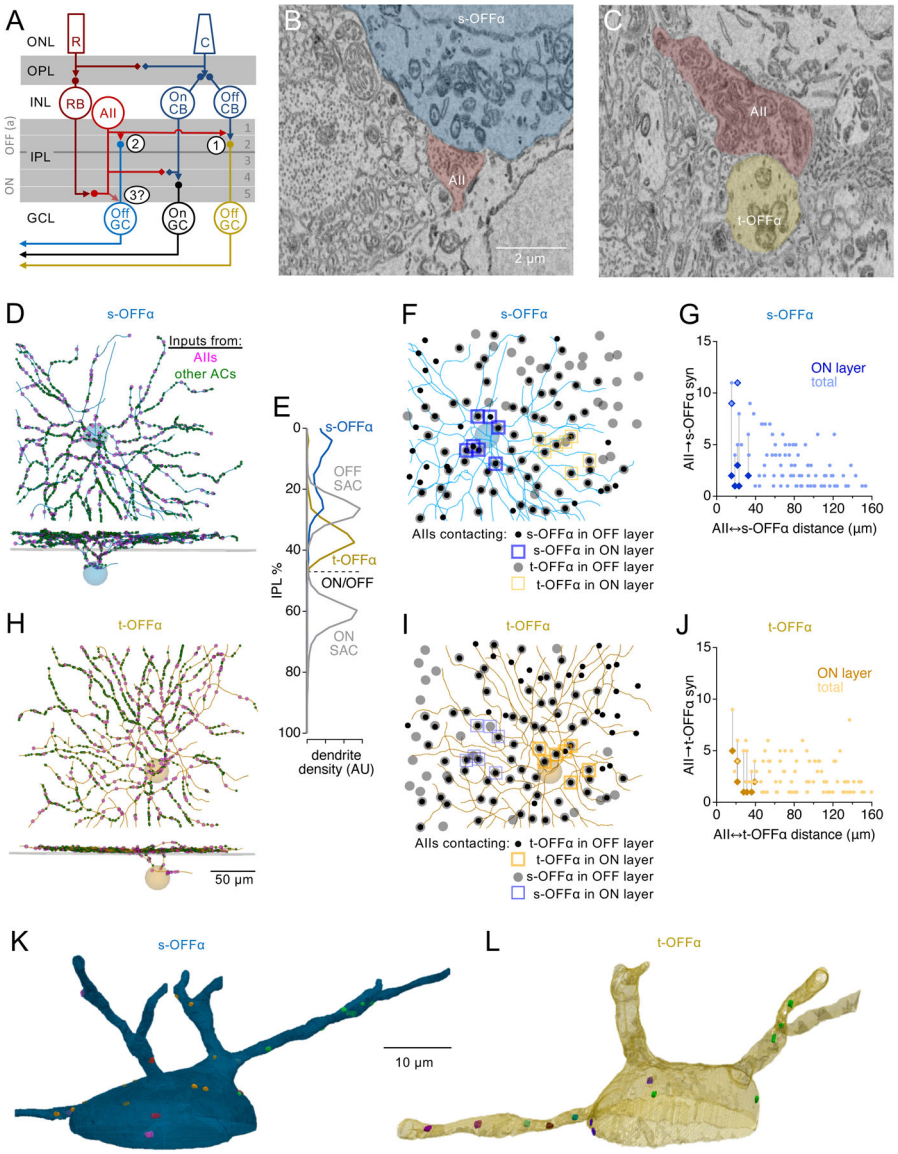

Figure 1 |. AII ACs make chemical synapses onto OFFα GC somas

(A) Retina schematic (modified[81]). ♦♦, gap junctions; ►●, chemical synapses. *1*, AII synapses onto OFF CB axon terminals; *2*, AII synapses onto OFF GC dendrites; *3*, proposed output synapses onto OFF GC somatic region. R, rod photoreceptor; C, cone photoreceptor; RB, rod bipolar cell, AII, AII amacrine cell; On CB, ON cone bipolar cell; Off CB, OFF cone bipolar cell; Off GC, OFF ganglion cell; On GC, ON ganglion cell; ONL, outer nuclear layer; OPL, outer plexiform layer; INL, inner nuclear layer; IPL, inner plexiform layer; GCL, ganglion cell layer.

(B-C) SBFSEM micrographs showing AII synapses onto a s-OFFα soma **(B)** and a t-OFFα dendrite **(C)**. Scale bar applies to **(B,C)**. See Figure S1 for serial EM sections. See Table S1 for quantitative summary.

(D) Skeletonized s-OFFα with all inhibitory inputs annotated. *Lower panel*, transverse view; gray plane indicates ON-OFF border in IPL[26]. See Figure S2 for annotated excitatory inputs.

(E) Histogram showing dendritic stratification of identified OFFαs in the EM dataset, relative to those of identified ON and OFF starburst amacrine cells (SACs).
(F) Soma locations of AIIs providing inputs to s-OFFα in the OFF (black circles) and/or ON layers (blue squares) of the IPL. Gray circles and gold squares indicate AIIs connected to the t- OFFα. See Figure S3 for inputs from other ACs.
(G) Summary plot showing the total synaptic contacts from AIIs to the s-OFFα versus retinotopic (*x-y*) distance between AII and GC somas. Diamonds indicate the number of ON/GCL contacts.
(H-J) As in **(D,F,G)** for the t-OFFα. Scale bar in **(H)** applies to **(D,F,H,I)**.
(K-L) 3D images of s-OFFα **(K)** and t-OFFα **(L)** GC somatic region. AIIs inputs are color-coded to indicate those arising from the same AII. Scale bar applies to both panels.
Please mention Figures S1-S3 and Table S1.

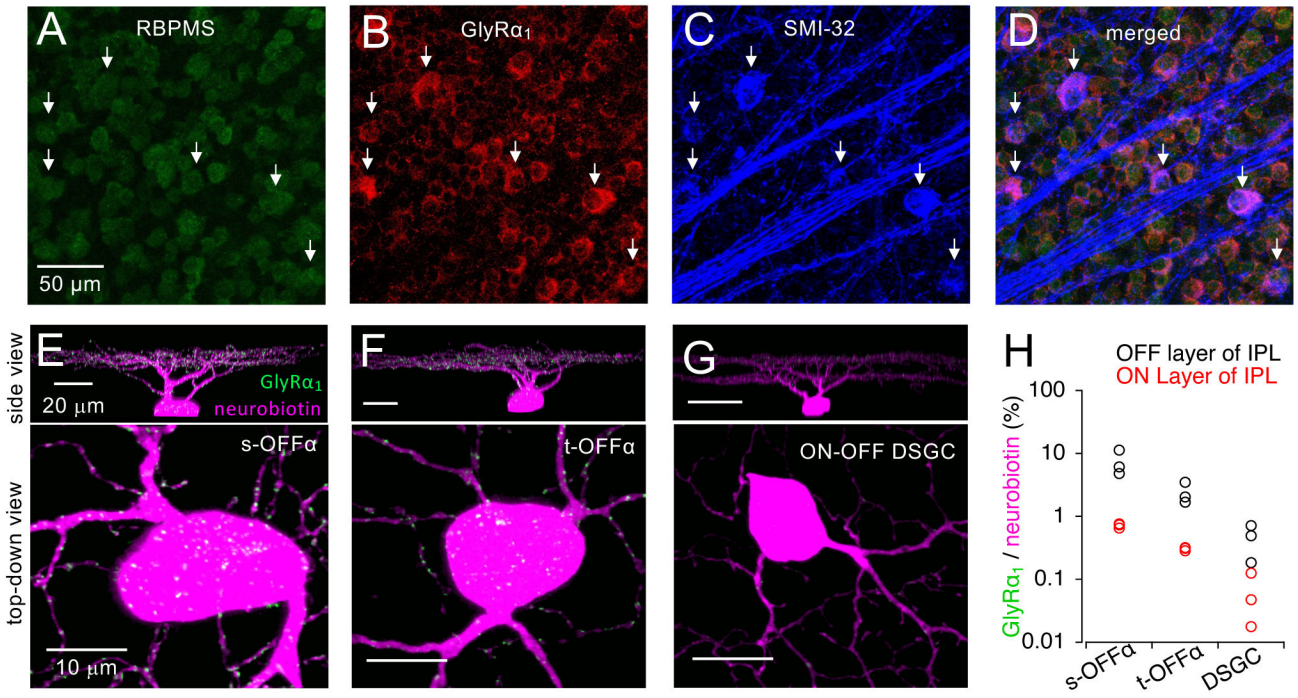

Figure 2 |. OFFα GCs express GlyRs densely in their somatic region

(A-D) Fluorescence micrographs of the GCL of a WT mouse retina incubated in antibodies to the GC marker RBPMS **(A)**, GlyRα$_1$ **(B)**, the αGC marker SMI-32 **(C)** and a merged image **(D)**. White arrows point to the same αGC somas in each panel. Scale bar in **(A)** applies to **(A-D)**.

(E-G) Side (*top*) and top-down (*bottom*) views of three neurobiotin (magenta) filled GCs (s-OFFα **(E)**, t-OFFα **(F)** and ON-OFF DS **(G)**) showing the GlyRα$_1$ signal (green) contained within a 3-D mask generated from the neurobiotin fill of the GC soma and proximal dendrites.

Magenta/green overlap appears white.

(H) Quantification of the GlyRα$_1$ signal (as a percentage of the neurobiotin signal) within the three GC types. The soma and the proximal dendritic arbor were included in the 'ON' arbor quantification, (n = 3 GCs of each type; n = 3 animals).

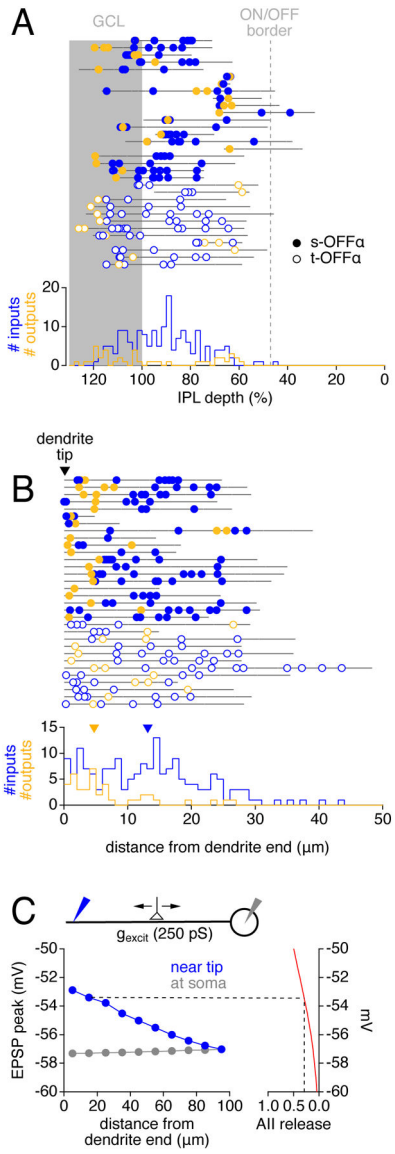

Figure 3 |. Localization of RB inputs and chemical synaptic outputs in AII arboreal dendrites

(A) Plot showing the IPL depth of 32 AII terminal dendrites making ON/GCL synapses onto the s-OFFα (closed gold circles) and t-OFFα (open gold circles). For clarity, dendrites are rendered as straight lines. Inputs from RBs indicated in blue. *Bottom*, histogram showing IPL depth of RB inputs and outputs to OFFαs.

(B) RB inputs and AII outputs shown as in (A), except that AII terminal dendrites have been straightened and aligned by their ends to compare linear distance along each dendrite between RB inputs (blue) and AII outputs to OFFαs (gold). *Bottom*, histogram showing locations of inputs and outputs relative to the dendrite terminus. Triangles indicate median values.

(C) Electrotonic model comparing simulated EPSPs, recorded near the end of the dendrite (blue) or at the soma (gray), evoked by an excitatory synaptic conductance at varying locations along the dendrite. *Right*, Simulated EPSPs projected onto an AII release function

derived from paired recordings between AIIs and type 2 CBs[14]. The release function indicates the fraction of readily releasable vesicles released vs. presynaptic membrane potential.

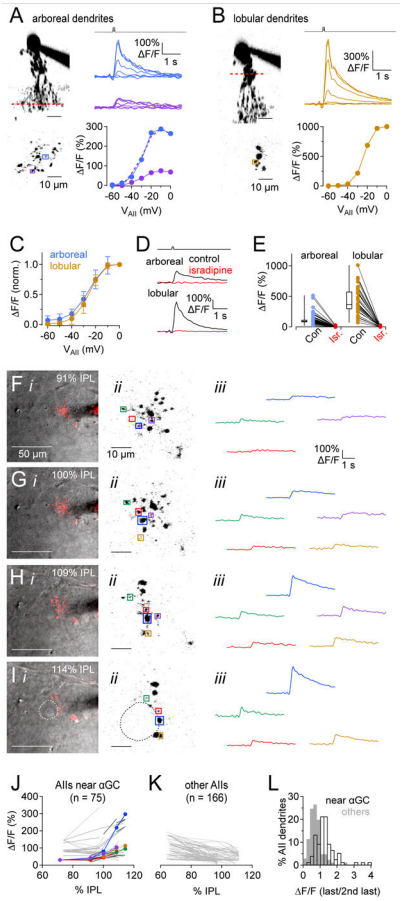

Figure 4 | Ca_V channel-mediated Ca^{2+} signaling in AII lobular and arboreal dendrites

(A) *Top left*, Fluorescence micrograph (*x-z* projection) of a recorded AII filled with Alexa 594 and Fluo 5F. Red line indicates focal plane of imaged varicosities. *Bottom left,* Squares indicate two typical varicosities imaged in a single *x-y* optical section. *Top right,* Average indicator ΔF/F signals in varicosities (colors correspond to squares, lower left) evoked by 100-ms voltage steps from −60 to 0 mV (10 mV increments, above). *Bottom right,* Indicator peak ΔF/F as a function of voltage step in the two varicosities. Dashed line show smaller responses scaled to facilitate comparison with the larger responses.

(B) *Top left*, Fluorescence micrograph of a recorded AII, similar to **(A)** except that the indicator imaging focal plane (red line) was in the lobular region. *Bottom left*, A square highlights a representative example of one lobular appendage in a single *x-y* optical section. *Top right*, Average indicator ΔF/F signals in a varicosity (indicated by square in lower left) evoked as in **(A)**. *Bottom right*, Indicator peak ΔF/F as a function of voltage step in the imaged varicosity.

(C) Voltage dependence of peak indicator ΔF/F signals in 103 arboreal (from 4 cells) and 29 lobular (from 3 cells) dendrites. Data in each varicosity were normalized to the ΔF/F signal evoked by a voltage step to 0 mV.

(D) Average indicator signals in arboreal and lobular dendrites evoked by a step to 0 mV in control conditions (black traces) and in the presence of Ca_V1 channel antagonist isradipine

(10 μM, red traces). Arboreal and lobular regions imaged in two different cells; control vs. isradipine comparisons were made in the same varicosities within each cell.

(E) Summary showing effects of isradipine on peak indicator signals in arboreal (n = 97) and lobular (n = 33) compartments of AIIs.

(F-I) Ca^{2+} indicator responses imaged in AII dendrites at four different focal planes in the IPL and GCL. *i*, fluorescence images of the Alexa 594-filled AII superimposed on a scanning DIC images of the tissue at the indicated depths relative to the top (0%) and bottom (100%) of the IPL, i.e., **(H-l)** were imaged in the GCL. Dashed circle in **(I)** indicates location of t-OFFα GC soma (see light responses in Figure S4). *ii*, fluorescence images of AII dendrites at indicated focal planes, with multiple ROIs indicated by squares. Squares of the same color correspond to the same dendrite at different depths. *iii*, indicator signals measured in corresponding ROIs at different depths. Not AII dendrites were recorded at AII depths.

(J) ΔF/F amplitudes as a function of IPL depth recorded from 75 dendrites in 4 AIIs located above αGCs. Each point represents a single ROI imaged at a particular IPL depth. Colors correspond to examples shown in **(F-I);** black lines are other dendrites from the imaged cell. Gray lines indicate ROIs from 3 other AIIs.

(K) ΔF/F amplitudes recorded from 166 dendrites in 6 different AIIs *not* located above an αGC.

(L) Histogram comparing ΔF/F amplitude in the last (most distal) ROI to the second-last ROI imaged in the same dendrites shown in **(J-K)**. Please mention Figure S4.

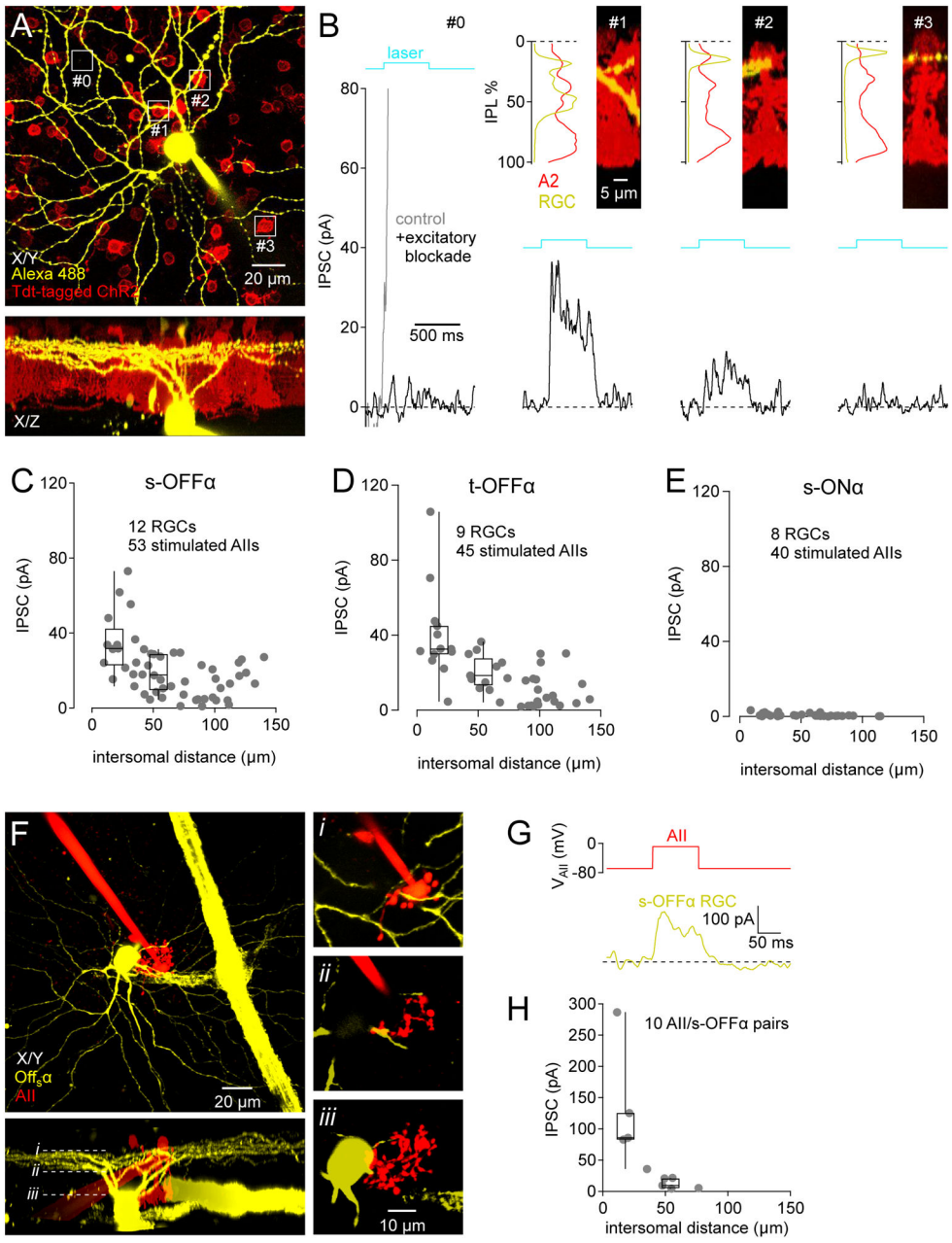

Figure 5 | Direct synaptic connections between AII ACs and OFFαs

(A) Fluorescence micrographs of an s-OFFα filled with Alexa 488 (yellow) in a retina expressing ChR and tdTomato under control of the NeuroD6 promoter.

(B) IPSCs (V_{hold} = +10 mV) evoked by laser stimulation directed to the areas indicated by white squares in **(A)**. Responses at location #0 (gray trace, *left*) reflect visual responses due to photoreceptor stimulation and were eliminated by blockers of bipolar cell activation. Additional panels show IPSCs (*bottom*) evoked by stimulating individual AIIs, which were identified morphologically by their dendritic ramification pattern in the IPL (*top*).

(C-E) Summary plots showing IPSC amplitudes recorded in s-OFFα **(C)**, t-OFFα **(D)** and s-ONα **(E)** GCs and evoked by ChR activation of AIIs, as a function of distance between

the AII and GC somas. Box plots in **(C)** and **(D)** compare median, range and quartiles of responses to AIIs located 0-36 μm and 36-72 μm from the recorded GC.

(F) Fluorescence micrograph showing a paired recording between a presynaptic AII (red) and a postsynaptic s-OFFα (yellow). White lines in lower (*x-z*) panel indicate focal planes shown in (*i-iii*). Scale bars apply to left and right panels, respectively.

(G) Averaged IPSC (V_{hold} = +10 mV) in s-OFFα shown in (F) evoked by step depolarization of the presynaptic AII.

(H) Summary data from 10 experiments showing the average IPSC amplitude vs. distance in the *x-y* plane between recorded cells.

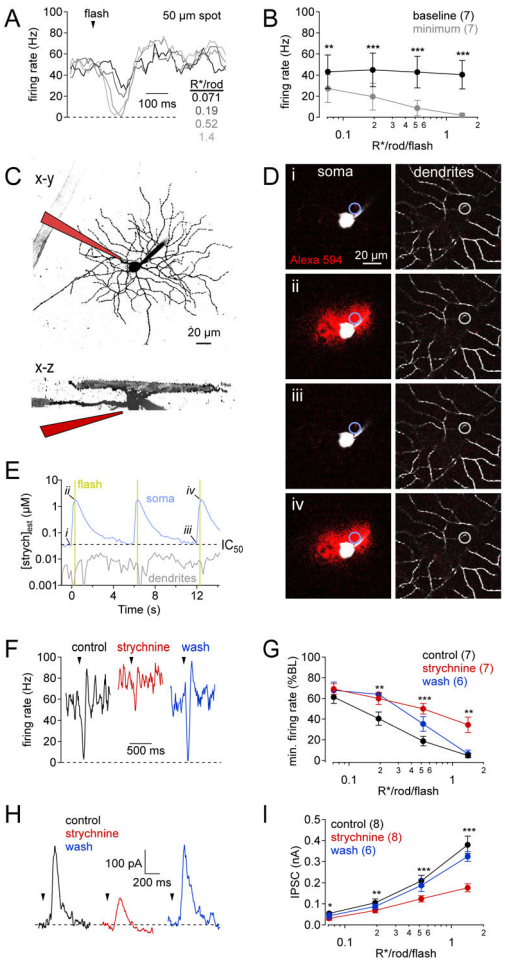

Figure 6 |. ON/GCL glycinergic inhibition influences OFFα GC light responses

(A) Spike frequency plot showing responses in an s-OFFα to brief (10-ms) light flashes of varying intensities.

(B) Summary data showing baseline and light-evoked minimum firing rates in 7 s-OFFαs. Asterisks indicate paired *t*-test comparisons between evoked and baseline rates at each intensity. ** = $p < .01$, *** = $p < .001$.

(C) Fluorescence micrograph of Alexa 488-filed s-OFFα, with approximate location of the strychnine puffer pipette indicated schematically. Scale bar (20 µm) applies to both views.

(D) Diffusion of Alexa 594 (red) from the puffer pipette, relative to an Alexa 488-filled s-OFFα (white) at the times indicated in **(E)**. Scale bars in (*i*) apply to lower panels. Circles indicate ROIs measured in **(E)**.

(E) Strychnine concentration at the soma (blue) and at the OFF layer dendrites (gray), estimated by the Alexa 594 signal relative to that in the puffer pipette. Timing of light flashes indicated in gold. Signals measured within the ROIs indicated in **(D)**.

(F) s-OFFα spike responses to light flashes (1.4 R*/rod) under control conditions (black), immediately following a strychnine puff (red), and following strychnine wash.

(G) Summary plot (n = 7) showing minimum firing rate, as a percentage of baseline, versus flash intensity under the different conditions described in **(F)**.

(H) Flash evoked IPSCs, recorded under the conditions described in **(F)**.
(I) Summary plot (n = 8) showing IPSC amplitude versus flash intensity under the conditions described in **(F)**.

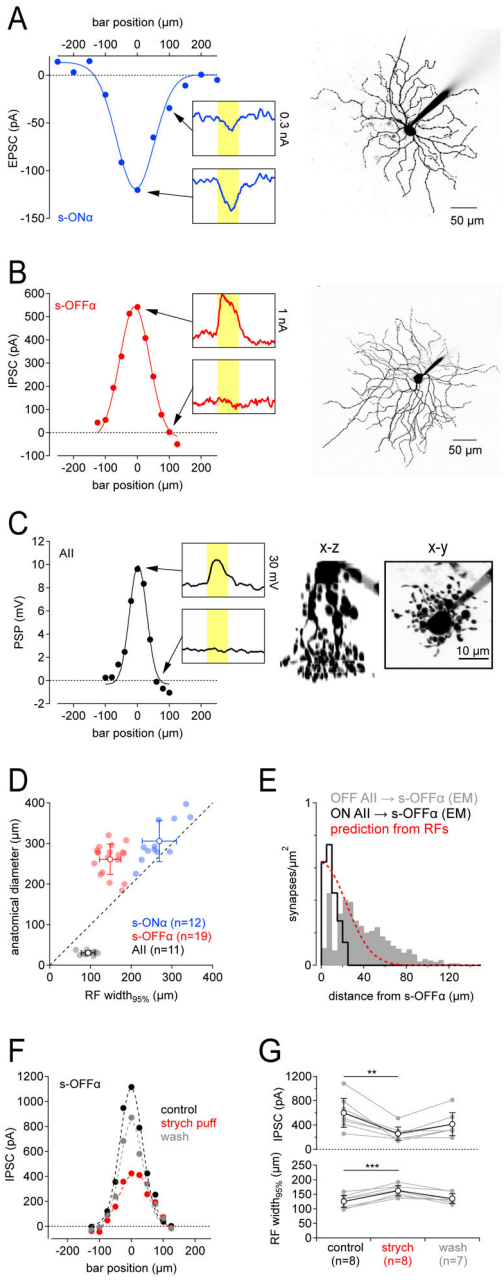

Figure 7 |. AII input condenses OFFα RFs

(A) EPSCs recorded from an s-ONα evoked by bars of light in different regions of its RF. *Right*, fluorescence micrograph of recorded cell.

(B) IPSCs recorded from an s-OFFα evoked by bars of light in different regions of its RF. *Right*, fluorescence micrograph of recorded cell. Also see Figure S5, which shows that blocking surround inhibition with TTX does not influence these RF measurements.

(C) PSPs recorded from an AII evoked by bars of light presented to different regions of its RF. *Right*, fluorescence micrograph (side and top views) of recorded cell.

(D) Summary plot comparing DF diameter and RF width in s-ONαs, s-OFFαs and AIIs. See Figure S6 for RF dimensions measured in photopic conditions.

(E) Histogram showing the spatial density distribution of AII → s-OFFα inputs in the OFF layer (gray) and ON layer (black), acquired from the EM dataset. Red dashed line indicates predicted spatial distribution of AII inputs to s-OFFαs based on the relative size of their RFs.

(F) IPSCs recorded from an s-OFFα evoked by bars of light in different regions of its RF in control (black), immediately following puff application of strychnine in the GCL (red), and following washout (grey).

(G) Summary graphs (n = 8) showing effects of local GCL strychnine puffs on s-OFFα IPSC amplitudes (*top*) and RF dimensions (*bottom*). **: $p = .002$; ***: $p = .00003$. Response recovery ("wash") was acquired in 7 of 8 cells. Please mention Figures S5 and S6.

KEY RESOURCES TABLE

REAGENT or RESOURCE	SOURCE	IDENTIFIER
Antibodies		
α-GlyRα$_1$ (rabbit monoclonal)	Synaptic Systems	146111
α-RBPMS (guinea pig polyclonal)	Phosphosolution	1832-RBPMS
α-SMI32 (mouse monoclonal)	Millipore Sigma	559844
streptavidin Alexa 568 conjugate	Invitrogen	S11226A
α-mouse (goat) Alexa 488	Invitrogen	PIA32723
α-guinea pig (donkey) Alexa 488	Jackson ImmunoResearch	706-545-148
α-rabbit (donkey) Cy3	Jackson ImmunoResearch	711-165-152
α-mouse (donkey) Cy5	Jackson ImmunoResearch	715-175-150
Chemicals, Peptides, and Recombinant Proteins		
Ames media	Millipore Sigma	A1420
$NaCHO_3$	Millipore Sigma	S5761
Cs methanesulfonate	Millipore Sigma	C1426
K methanesulfonate	Millipore Sigma	83000
TEA-Cl	Millipore Sigma	T2265
Mg ATP	Millipore Sigma	A9187
Na GTP	Millipore Sigma	G8877
EGTA	Millipore Sigma	E8145
Na_2 phosphocreatine	Millipore Sigma	P7936
HEPES	Millipore Sigma	H3375
AlexaFluor 594	Thermo Fisher	A10438
Fluo-5F	Thermo Fisher	F14221
DNQX	abcam	120169
R-CPP	Tocris	0247
L-AP4	abcam	120002
UBP 310	abcam	120168
NBQX	abcam	120046
D-AP5	Tocris	0106
strychnine	Millipore Sigma	S0532
Deposited Data		
SBFSEM data set	Kevin Briggman	k0725
Experimental Models: Organisms/Strains		
mouse: wild-type: C57BL/6J	Jackson Laboratory	000664
mouse: Neurod6-Cre: C57BL/6-*Hprt*$^{tm333(Ple281\text{-}icre/ERT2)Ems}$/Mmjax	Jackson Laboratory	037063
mouse: Ai27: B6.Cg-*Gt(ROSA)26Sor*$^{tm27.1(CAG\text{-}COP4*H134R/tdTomato)Hze}$/J	Jackson Laboratory	012567
Software and Algorithms		
Symphony	https://symphony-das.github.io/	